Measurement of Cell Density and Necrotic Fraction in Human Melanoma Xenografts by Diffusion Weighted Magnetic Resonance Imaging

Heidi Lyng,[1*] Olav Haraldseth,[2] and Einar K. Rofstad[1]

The aim of this study was to investigate whether apparent diffusion coefficients (ADCs) could be used as measures of cell density and necrotic fraction of tumors. Tumors of four human melanoma xenograft lines were subjected to diffusion-weighted magnetic resonance imaging (DWI). ADCs were calculated from the images and related to cell density and necrotic fraction, as determined from histological sections. A significant correlation was found between the ADC of the viable tissue and cell density, regardless of whether tumors of different lines or different regions within individual tumors were considered. Necrosis was found in two of the lines. A single region of massive necrosis that could be differentiated from the viable tissue in ADC maps was found in one line, whereas a number of smaller necrotic regions that could not be identified in ADC maps were found in the other line. Tumor ADC was significantly correlated with the necrotic fraction of the former, but not of the latter line. Our results suggest that ADCs can be used as measures of cell density and necrotic fraction of some but not of all tumors, depending on whether the individual necrotic regions are large enough to be differentiated from the viable tissue with the obtained spatial resolution of the DW images. Magn Reson Med 43:828–836, 2000. © 2000 Wiley-Liss, Inc.

Key words: diffusion-weighted MRI; cell density; necrosis; melanoma xenograft

MRI is often used to obtain information on macroscopic structures in the body, such as the anatomic extension of tumors, and is, therefore, a useful diagnostic tool in cancer therapy. Information on microscopic structures in tissues, such as the cell density and necrotic fraction of tumors, would, however, also be useful. The cell density may be indicative of tumor aggressiveness; several clinical studies suggest an increased metastatic capacity of highly cellular tumors (1–3). Necrosis is associated with an acidic microenvironment and a low oxygen concentration (4); features that may influence the response to e.g., radiotherapy, hyperthermia, and chemotherapy (5,6). Moreover, changes in cell density and necrotic fraction during and after treatment may reflect tumor response (7). Methods for measurement of cell density and necrosis in tumors may, therefore, be used to tailor therapy for individual patients and to monitor tumor response to therapy (8–10).

Diffusion-weighted magnetic resonance imaging (DWI) can be used to monitor cellular structures in biological media and has been suggested as a tool to distinguish different tissue compartments (11). Through the application of strong gradients in the imaging sequence, imaging is sensitized to the displacement of spins of diffusing protons. Mainly protons of bulk water and not protons within macromolecules and membranes or water protons bound to macromolecules and membranes contribute to the signal in DW images, because the latter protons are relatively immobile and have extremely short T_2 values (12). The apparent diffusion coefficient (ADC) of water can be calculated from the images, where apparent refers to the fact that these values are based on water protons experiencing different restrictions to diffusion inside several tissue or cellular compartments in a single voxel (11,12). The ADC depends on the presence of diffusion barriers, such as cell membranes and macromolecules, in the water microenvironment. Compartments with different cellular structures may, therefore, exhibit different ADCs and be identified in ADC maps.

Previous studies suggest that this technique may have a potential for registration of cell density and necrosis in tumors. Much knowledge of tissue ADCs has come from experimental studies investigating the usefulness of DWI to detect early effects of ischemia on brain tissue (e.g., 13–18). A reduction in ADC up to 50% occurs immediately after induction of ischemia. Several reasons for this reduction have been proposed; e.g., swelling of cells, leading to changes in the relative volume of the intra- and extracellular compartments, and interruption of molecular movement in the intracellular compartment due to energy depletion during cell injury (14,15). The factors important for ADCs of tumors may, however, be different from those determining the ADCs of normal tissues. Several studies have shown changes in tumor ADC after treatment that occurred before changes in tumor volume were detected, suggesting that the changes in ADC could be an early indication of response (8–10). An elevated ADC of necrosis and edema compared to viable tumor tissue has been reported (19–23), showing that necrosis and edema can be differentiated from the viable tissue based on ADCs. Moreover, Sugahara et al. (24) reported recently a correlation between the minimum ADC of tumor regions and cell density in human gliomas; regions with high cell density had lower ADC than regions with low cell density. Another study on human gliomas found an inverse correlation between the choline signal intensity, measured by proton MR spectroscopy, and the ADCs, suggesting a relationship between tumor ADC and cellularity (25,26). More detailed studies relating ADCs to cell density and necrotic fraction in tumors outside the brain are needed to fully understand the usefulness of DWI for registration of cell density and necrosis.

[1]Department of Biophysics, The Norwegian Radium Hospital, Oslo, Norway.
[2]MR Centre, SINTEF/UNIMED, Trondheim, Norway.
*Correspondence to: Heidi Lyng, Department of Biophysics, The Norwegian Radium Hospital, Montebello, 0310 Oslo, Norway.
Received 2 July 1999; revised 27 January 2000; accepted 28 January 2000.

In the present work tumors of four different human melanoma xenograft lines were subjected to DWI. ADC maps were generated from the images and used to determine tumor ADC and the ADC of necrosis and viable tissue. The aim was to investigate to what extent the ADCs could be used to obtain information on cell density and necrotic fraction of tumors. Cell density and necrotic fraction were determined by histological analyses of tumor sections. The four melanoma lines were well suited for the present purpose; they differed significantly with respect to cell density and pattern of necrosis.

MATERIALS AND METHODS

Mice and Tumor Lines

Female BALB/c-*nu/nu* mice, 8 to 10 weeks old and 20 to 30 g of weight, were used. The mice were bred at the animal department of our institute and kept under specific-pathogen-free conditions at constant temperature (24–26°C) and humidity (30–50%). Sterilized food and tap water were given ad libitum.

Four amelanotic human melanoma xenograft lines were included; A-07, D-12, R-18, and U-25 (27). Xenografted tumors were initiated from exponentially growing monolayer cultures in passages 75–100. Monolayer cells, cultured in RPMI-1640 medium supplemented with 13% fetal calf serum, 250 mg/L penicillin, and 50 mg/L streptomycin, were detached by trypsinization. Approximately 2.5×10^5 A-07 cells or 5.0×10^5 D-12, R-18, or U-25 cells in 10 μl of Ca^{2+} - and Mg^{2+} - free Hanks balanced salt solution were inoculated intradermally in the mouse leg. Tumors were grown to diameters in the range of 4 to 13 mm before they were used, corresponding to volumes in the range of 50 to 360 mm^3 for all but one tumor with a volume of 1000 mm^3. Five tumors of each line (volumes 140–360 mm^3, A-07; 160–210 mm^3, D-12; 120–280 mm^3, R-18; 50–1000 mm^3, U-25), were used in the study of ADC against cell density, whereas 8 D-12 tumors (volumes 100–225 mm^3) and 8 U-25 tumors (volumes 50–1000 mm^3) were used to study ADC against necrotic fraction.

Diffusion-Weighted Magnetic Resonance Imaging

DWI was performed in the axial plane of the tumors by use of a 2.35 T Bruker Biospec (Bruker, Karlsruhe, Germany) with a bore size of 40 cm. The mice were kept under general anesthesia during imaging. The anesthetic consisted of 80% Sombrevin (Gedeon Richter, Budapest, Hungary), 12% Hypnorm Vet (LEO, Helsingborg, Sweden), and 8% Stetsolid, 5 mg/mL (Dumex, Copenhagen, Denmark), and was administered i.p. in doses of 0.01 mL/g body weight. The mice were positioned on an imaging cradle fitted with a specially designed saddle coil. A bed containing fluorocarbons circulating in a closed chamber was used to avoid excessive heat loss from the body. Measurement of rectal temperature in a few animals verified that the body temperature was maintained at 37°C by use of this procedure.

The tumors were positioned in the isocenter of the magnet. The field homogeneity was optimized by performing global shims at the start of imaging. A sagittal scan was used for tumor localization and to determine the position of the axial scan. The axial scan consisted of 6 to 8 slices, covering the whole tumor. Diffusion weighting was achieved by using a multislice pulsed gradient spin echo sequence (TE/TR: 28 s/1500 s) with 5 different gradient strengths. The time between the start of each gradient pulse (Δ) was 10 s, and the duration of the gradient pulses (δ) was 7 s, leading to an effective diffusion time (Δ-δ/3) of 8 s (11). A series of 5 diffusion-weighted images, one image of each gradient strength, were obtained for each slice. The gradient strengths (G) ranged from 75 mT/m to 185 mT/m, and the diffusion encoding constant [$b = \gamma^2 \cdot G^2 \cdot \delta^2 \cdot (\Delta - \delta/3)$, where γ is the gyromagnetic ratio] ranged from 150 s/mm^2 to 925 s/mm^2. Gradients in the *z*-direction, parallel to the mouse leg, were used. Additional images with gradients in the *x*-direction were obtained of four tumors to ensure that the ADCs were not dependent on gradient direction. The images were acquired with a 3 × 3 cm field of view, a 128 × 128 image matrix, a slice thickness of 1 mm, and a slice gap of 1.2 mm, leading to an in plane resolution of 0.23 × 0.23 mm and a voxel size of 0.055 mm^3. Two excitations were employed. The total examination time, including setup, tumor localization, and DWI, was approximately 30 min.

Imaging of a water phantom at 37°C was performed as described above to verify that the imaging technique gave reliable ADC values. The ADC of the phantom was 3.0×10^{-3} mm^2/s, which is consistent with literature values of approximately 2.3×10^{-3} mm^2/s for water diffusion coefficients at 25°C (28), taking into account an increase in the diffusion coefficient of 2.4% per °C (11).

Image Analysis

The images were transferred to a Macintosh computer and analyzed using the public domain program Image, Version 1.45 (Wayne Rasband, National Institutes of Health, Bethesda, MD). ADC maps were generated for each slice on a pixel-by-pixel basis from the signal intensity of the five DW images and the corresponding *b*-values:

$$S(b) = S(0) \cdot e^{-b \cdot \mathrm{ADC}} \quad [1]$$

where $S(b)$ is the signal intensity achieved with diffusion encoding constant b, and S (0) is the signal intensity achieved without gradient (11). Thus, the natural logarithm of the signal intensities were plotted against the *b*-values, and the ADCs were calculated as the slope of linear curves fitted to these plots. The fits generally had a correlation coefficient of approximately 0.99. Image artifacts caused by movement of the mice during imaging led to lower correlation coefficients. MR examinations, in which movement had occurred, could easily be identified due to the low correlation coefficients. These examinations were excluded from the analyses. The ADC maps of the three most centrally located slices were included in the further analyses, since histological sections in planes corresponding to these slices were obtained (see Histological Sections). Regions of interest (ROIs) were drawn with a cursor in the ADC maps, using the corresponding histological section to identify the regions. ADC histograms were generated for each ROI.

Histological Sections

The orientation of the tumors was marked on the surrounding skin after imaging. The tumors were excised, fixed in 4% formalin, and cut into three sections with a thickness of 5 μm. The localization of the sections corresponded to the central part of the three most centrally located MR slices. The sections were stained with hematoxylin and eosin and analyzed by use of a light microscope (Sony DXC-151P, Sony Norge, Oslo, Norway) connected to a computer based image analysis system (KS300, Kontron Elektronik GmbH, München, Germany).

Cell Density and Necrotic Fraction

Cell density was determined by use of the method described by Brammer and Jung (29). Briefly, the number of nuclei per unit of tissue volume, *Nv*, was used as a measure of cell density and was derived from the formula

$$N_v = \frac{V_v}{v} \quad [2]$$

where, V_v is fraction of tissue volume occupied by nuclei, and v is the nuclear volume. Color images of the viable tumor tissue were transferred to the computer. The magnification of the images, as shown on the monitor, was 1250×. Grids were superimposed on the images. First, a grid of 9 horizontal lines was used. The chord lengths, i.e., lengths of each line segment running inside a nuclear profile, were measured interactively by using a cursor to define the chords. At least 30 chords were measured in each image. The mean chord length, l, was used to calculate the mean nuclear diameter, d, of each image:

$$d = \frac{3}{2} l \quad [3]$$

assuming the nuclei to be spherical and of equal size, and the section thickness to be infinitely thin. Thereafter, a grid of 117 test points was used. The frequency of points hitting nuclear profiles, P_p, was determined interactively by using a cursor to define the hits. The values of d and P_p were used to calculate V_v and v in Eq. [2]:

$$V_V = P_p \cdot \left(1 + \frac{3 \cdot t}{2 \cdot d}\right)^{-1} \quad [4]$$

where t is the section thickness (5 μm). The third power of l was used as an estimate of v.

The necrotic fraction was calculated from the formula:

$$F_n = \frac{A_n}{A_t} \quad [5]$$

where F_n is necrotic fraction, A_n is area of necrosis, and A_t is total tumor area. Color images covering the whole sections were transferred to the computer. The magnification of the images, as shown on the monitor, was 130×. A_n and A_t were measured interactively by using a cursor to define the areas.

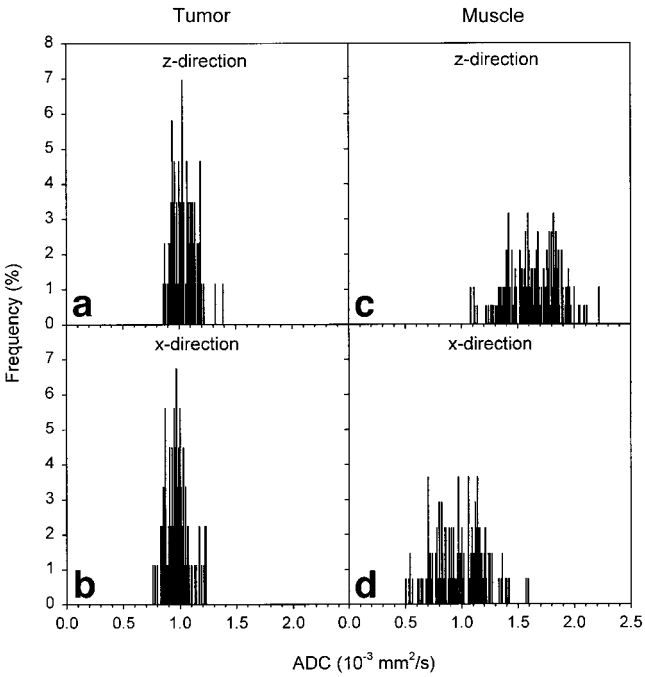

FIG. 1. ADC histograms of an A-07 human melanoma xenograft tumor (**a, b**) and a mouse leg muscle (**c, d**). The values in **a** and **c** are achieved with gradients in *z*-direction, whereas the values in **b** and **d** are achieved with gradients in *x*-direction.

Statistical Analysis

Kolmogorov-Smirnov distances were considered to determine whether the ADCs were normally distributed. Normal distributions were always achieved when the viable and necrotic tissue were analyzed separately. The mean value was, therefore, used to describe the ADC of these tissues. A *t*-test or a Mann-Whitney rank sum test was used to search for differences between two ADC histograms. Significant correlation between two parameters was searched for by Pearson product moment correlation analysis. A significance level of $P = 0.05$ was used throughout.

RESULTS

ADCs based on DW images acquired with gradients in *z*- and *x*-directions were compared for one tumor of each line. There was no significant difference in the ADCs achieved by using different gradient directions, regardless of which tumor was considered ($P > 0.05$). This is illustrated in Fig. 1, showing ADC histograms of an A-07 tumor, using gradients in *z*- (a) and *x*-directions (b). Thus, the ADCs were not dependent on gradient direction, suggesting isotropic diffusion of water in these tumors. The use of a single gradient direction was therefore justified. In contrast, the ADCs of muscular tissue were highly dependent on gradient direction (Fig. 1c, d). Thus, higher ADCs were achieved with gradients in the *z*-direction, parallel to the mouse leg, than with gradients in the x-direction, perpendicular to the mouse leg, reflecting the anisotropic diffusion of water in muscular tissue (30).

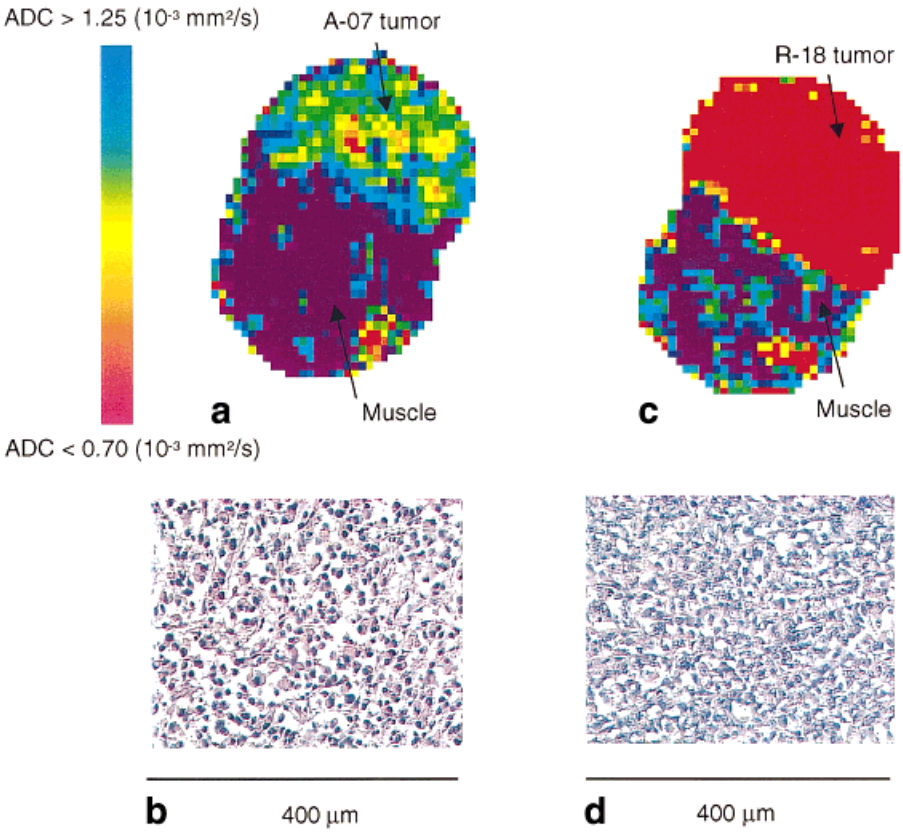

FIG. 2. ADC map (**a, c**) and HE stained histological section (**b, d**) of an A-07 (**a, b**) and R-18 (**c, d**) human melanoma xenograft tumor. The ADC maps are from a plane through the central part of the tumors and show the ADCs of tumor and leg muscle. Red pixels represent ADC values below 0.70 $\times$ 10^{-3} mm^2/s, whereas lilac pixels represent ADC values above 1.25 $\times$ 10^{-3} per mm^2/s. The cell density of the sections was 1.8 $\times$ 10^5 per mm^3 (**b**) and 5.4·10^5 per mm^3 (**d**).

ADC and Cell Density

The cell density of the viable tumor tissue differed considerably among the lines. A-07 and U-25 tumors had the lowest cell densities (mean $\pm$ SE) of 1.9 $\times$ 10^5 $\pm$ 0.1 $\times$ 10^5 per mm^3 and 2.1 $\times$ 10^5 $\pm$ 0.3 $\times$ 10^5 per mm^3, respectively, R-18 tumors had the highest cell density of 4.4 $\times$ 10^5 $\pm$ 0.5 $\times$ 10^5 per mm^3, whereas D-12 tumors had intermediate cell density of 3.2 $\times$ 10^5 $\pm$ 0.2 $\times$ 10^5 per mm^3. There was a significant correlation between cell density and tumor volume of the R-18 line ($r = 0.95$, $P = 0.01$), but not of any of the other lines.

ROIs including the viable tumor tissue were selected in the ADC maps, using the corresponding histological sections to identify the regions. ADC histograms of the viable tissue were generated for each tumor and used to calculate the mean ADC of each line. The ADC of the viable tissue differed among the lines and was (mean $\pm$ SE) 0.98 $\times$ 10^{-3} $\pm$ 0.03 $\times$ 10^{-3} mm^2/s (A-07), 0.86 $\times$ 10^{-3} $\pm$ 0.02 $\times$ 10^{-3} mm^2/s (D-12), 0.81 $\times$ 10^{-3} $\pm$ 0.03 $\times$ 10^{-3} mm^2/s (U-25), and 0.65·$10^{-3}$$\pm$0.02·$10^{-3}$ mm^2/s (R-18). Thus, tumors of the line with low cell density had high ADC compared to tumors of the line with higher cell density. This is illustrated in Fig. 2, showing ADC maps and histological sections of the viable tissue of an A-07 tumor (a, b) and an R-18 tumor (c, d). The ADC histograms of the two tumors are shown in Fig. 3. The A-07 tumor had higher ADC and lower cell density than the R-18 tumor. There was no necrosis in these tumors.

A significant correlation was found between ADC of the viable tissue and cell density when tumors of all lines were included in the analysis (Fig. 4a) ($r = -0.71$, $P = 0.0004$); the ADC decreased linearly with increasing cell density. To investigate whether there was a significant correlation between ADC and cell density within individual tumors, the parameters were determined for several regions within the same tumor. An A-07 tumor with large differences in cell density was used for this analysis. Eight regions (0.8 – 1.9 mm^2, each with approximately homogeneous cell density, were selected within the tumor for determination of cell density and ADC. A significant correlation between the two parameters was found ($r = -0.84$, $P = 0.008$) (Fig. 4b); tumor regions with low cell density had high ADC compared to regions with high cell density. The ADC showed a significant correlation to tumor volume of the R-18 line; i.e., the line with a significant correlation between cell density and tumor volume. There was no correlation between ADC and tumor volume of the other lines.

ADC and Necrosis

Two of the lines, D-12 and U-25, developed necrosis when growing to the tumor volumes used here. The necrotic

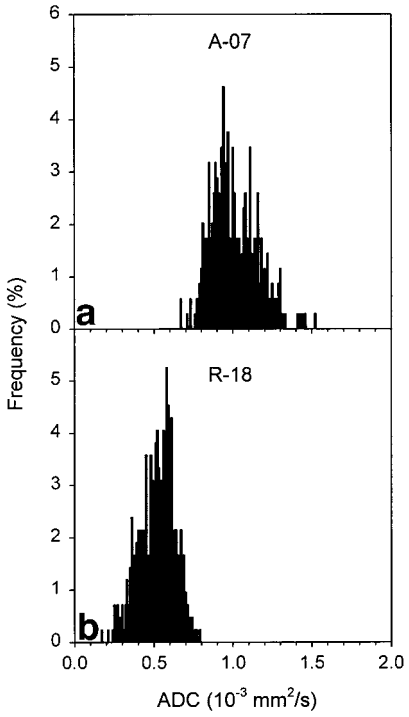

FIG. 3. Tumor ADC histograms generated from the ADC maps depicted in Fig. 2; i.e., from a plane through the central part of an A-07 (**a**) and R-18 (**b**) human melanoma xenograft tumor.

pattern differed considerably between these lines. The D-12 line developed a single region of massive necrosis originating from the central part of the tumors, whereas the U-25 line developed a number of smaller necrotic regions distributed throughout the tumors. There was a significant correlation between necrotic fraction and tumor volume of the D-12 line ($r = 0.90$, $P = 0.002$), but not of the U-25 line ($r = 0.23$, $P = 0.59$). The necrotic regions of the D-12 tumors could easily be identified in ADC maps; the ADC of the necrotic regions was elevated compared to the ADC of the surrounding viable tissue. This is illustrated in Fig. 5 a and b, showing the ADC map and histological section of a D-12 tumor with a large necrotic region. The ADC histogram of the tumor is shown in Fig. 6a. Necrotic D-12 tumors had a broad ADC histogram, caused by the large difference in ADC between the viable and necrotic tissue, and a high mean ADC value compared to D-12 tumors without necrosis. ROIs including solely viable tissue or necrosis were selected in ADC maps of the D-12 tumors, using the corresponding histological sections to identify the regions. Pooled ADC histograms of the viable and necrotic tissue are shown in Fig. 7a and b, respectively. The ADC of necrosis was significantly higher than that of the viable tumor tissue ($P < 0.001$). In contrast to these observations, the necrotic regions of the U-25 tumors were not easily differentiated from the viable tissue in ADC maps. This is illustrated in Fig. 5c and d, showing the ADC map and histological section of a U-25 tumor with several necrotic regions, most of them less than 1×1 mm in size, distributed throughout the tissue. Thus, the ADC histogram of the tumor was not particularly broad, even though the necrotic fraction was relatively high (Fig. 6b). Similar results were achieved for all necrotic U-25 tumors. It was, therefore, not possible to identify the necrotic regions of these tumors in the ADC maps.

ROIs including the entire tumor were selected in the ADC maps, and tumor ADCs were calculated. Figure 8 shows plots of the tumor ADC of individual MR slices (including viable and necrotic tissue) against the necrotic fraction of the corresponding histological sections of the D-12 and U-25 lines separately. The relationship between the two parameters differed between the lines. D-12 tumors showed a significant correlation between ADC and necrotic fraction ($r = 0.73$, $P < 0.0001$); tumors with high necrotic fraction had high ADC compared to tumors with low necrotic fraction. In contrast, no such correlation was found for U-25 tumors ($r = 0.02$, $P = 0.91$); tumors with high necrotic fraction in general, did not have higher ADC than tumors with low necrotic fraction.

DISCUSSION

The present work, investigating the relationship between tumor ADC on the one hand and cell density and necrotic fraction on the other, was based on the hypothesis that tissues with different cell density or necrotic fraction exhibit different ADC values due to a different content of diffusion barriers. This hypothesis was plausible, since the

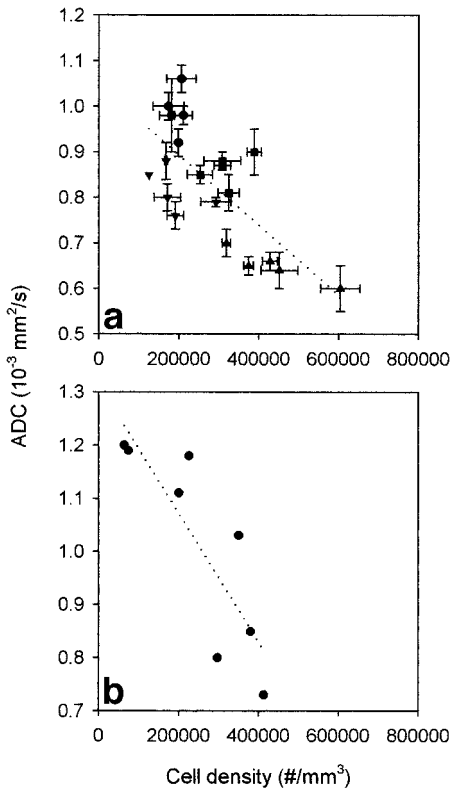

FIG. 4. ADC of the viable tissue versus cell density of human melanoma xenograft tumors (**a**) and of an individual A-07 human melanoma xenograft tumor (**b**). In **a** each point represents mean ± SE of a single tumor. ●, A-07 tumors; ■, D-12 tumors; ▲, R-18 tumors; ▼, U-25 tumors. In **b** each point represents ADC and cell density of a region (0.8 – 1.9 mm^2 within the tumor. The stippled curves are fitted to the data by linear regression analysis.

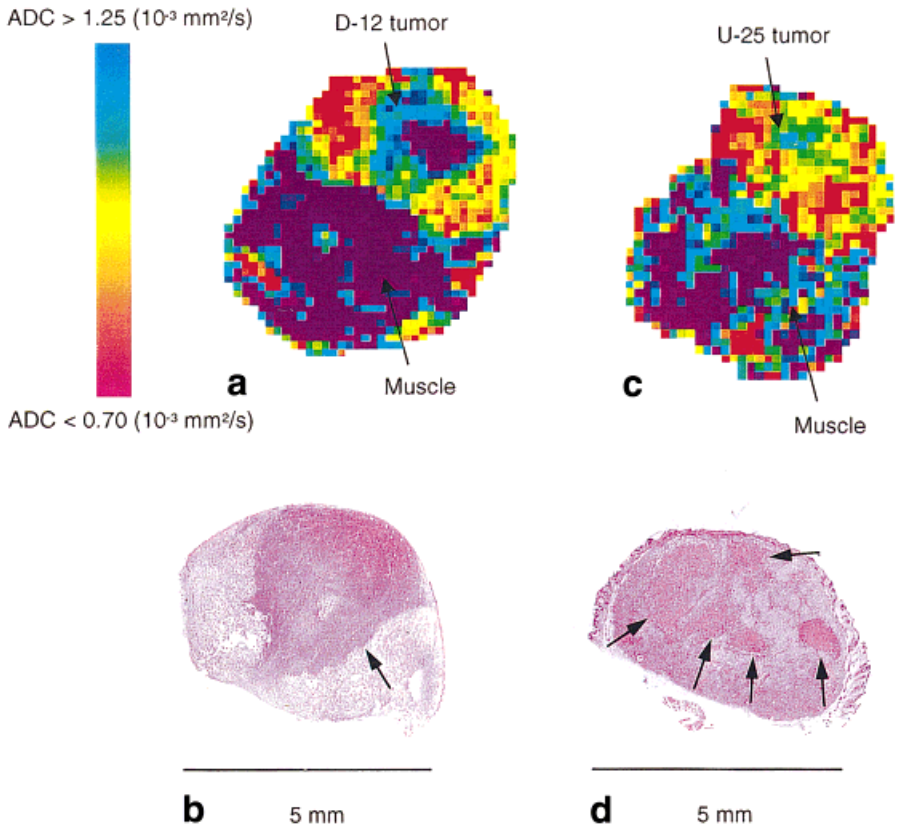

FIG. 5. ADC map (**a, c**) and HE stained histological section (**b, d**) of a D-12 (**a, b**) and U-25 (**c, d**) human melanoma xenograft tumor. The ADC maps are from a plane through the central part of the tumors and show the ADCs of tumor and leg muscle. Red pixels represent ADC values below 0.70 $\times$ 10^{-3} mm^2/s, whereas lilac pixels represent ADC values above 1.25 $\times$ 10^{-3} per mm^2/s. In the histological sections arrows point to necrosis. The necrotic fraction of the sections was 0.38 (**b**) and 0.22 (**d**).

cell and nuclear membranes are the most important diffusion barriers in tumors. Thus, although some water exchange across the membranes may occur during image acquisition, the membranes are relatively impermeable to water and cause significant restrictions to diffusion (12). In addition to the membranes, the intracellular cytoskeleton, organelles, matrix fibers, and soluble macromolecules contribute to diffusion restrictions in tumors.

Measurement of ADCs reflecting the cell density and necrotic fraction of tumors necessitates the use of a diffusion time long enough for most water molecules to hit the membranes during image acquisition (31). This condition is met if the free diffusion length of the water molecules, l_d, is defined as $(2 \cdot D_0 \cdot t)^{1/2}$ where D_0 is the free water diffusion coefficient of the tissue fluid, and t is the diffusion time, is on the order of or longer than the distance between the membranes (32). A diffusion time of 8 ms was used in the present work. Assuming a value of 3.0 $\times$ 10^{-3} mm^2/s for D_0, this leads to a free diffusion length of about 7 μm. The nuclear radius, as determined from Eq. (3) in this study, differed little among the tumor lines and was about 5 μm, suggesting that the diffusion time was probably long enough for the water molecules to hit the intracellular membranes. Based on the cell densities found here, it can be assumed that the diffusion time also was long enough for the water molecules to hit the membranes in the extracellular compartment. Although longer diffusion times have been recommended in ADC studies on tumors (33), a diffusion time of 8 ms was found to be long enough to achieve significant differences in ADC between the tissue types. The advantage of using such a short diffusion time is achievement of reduced TE and improved signal to noise ratio in the images.

A significant correlation was found between the ADC of the viable tumor tissue and cell density; the ADC decreased with increasing cell density. The correlation existed regardless of whether tumors of different lines or regions within individual tumors were considered. A similar relationship between the minimum ADC and cell density was also found in a recent study on human gliomas (24), suggesting that the ADC of the viable tumor tissue is mainly determined by the cell density.

The ADC of viable tissue can be regarded as the result of roughly independent contributions from the intra- and extracellular compartment (12,15). There may, therefore, be at least two factors contributing to a decrease in ADC with increasing cell density. Firstly, tissues with high cell density have a large fraction of intracellular water compared to tissues with low cell density. The intracellular water has presumably lower ADC than the extracellular water due to a higer content of diffusion barriers in the intracellular compartment (12). This leads to a lower ADC

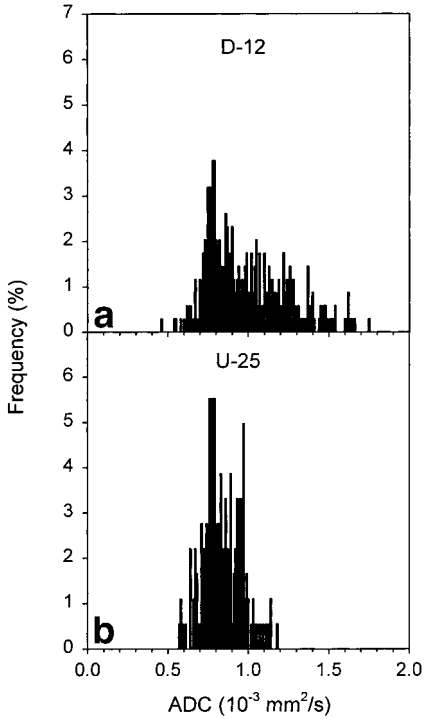

FIG. 6. Tumor ADC histograms generated from the ADC maps depicted in Fig. 5; i.e., from a plane through the central part of a D-12 (**a**) and U-25 (**b**) human melanoma xenograft tumor.

for highly cellular tissues. Secondly, tissues with high cell density have a small extracellular compartment compared to tissues with low cell density. The mobility and, hence, the ADC of the extracellular water are, therefore, decreased in the former tissues, leading to lower ADC. The influence of this factor is strengthened because the ADC is biased towards the diffusion coefficient of the compartment with the longest T_2; i.e., the extracellular compartment (12). Both factors are probably highly relevant for explaining the relationship between ADC and cell density observed here. Studies performed earlier in our laboratory show that cell volume differed little among the tumors (unpublished results). A high cell density was therefore probably associated with a small extracellular volume rather than a small volume of individual cells. In fact, our previous measurements of the extracellular volume of A-07 and R-18 tumors by use of contrast enhanced MR imaging show that the former tumors have a significantly larger extracellular volume than the latter (34), consistent with the lower cell density of these tumors. Other factors, although less likely, may also contribute to a decrease in ADC with increasing cell density, such as decreased membrane permeability in tissues with high cell density.

Necrotic fraction was significantly correlated with tumor ADC of the D-12 line but not of the U-25 line. Thus, the ADC of D-12 tumors increased with increasing necrotic fraction, due to the increased ADC of necrotic compared to viable tissue. An elevated ADC of necrotic regions has also been reported by others (19–23, 33), and reflects increased mobility of water in the necrotic tissue. In fact, as a hypothesis the ADC of massive necrosis can be regarded as the ADC of viable tissue with zero cell density; the ADC of necrosis was consistent with the value achieved when extrapolating the linear fit of ADC against cell density to zero cell density (Figs. 4a and 7). In contrast to the D-12 tumors, the U-25 tumors showed no increase in ADC with increasing necrotic fraction. Uncertainties in the method used to determine necrotic fraction may have contributed to this observation. Thus, our results should be confirmed using other methods, based on e.g., contrast-enhanced MRI (35) or advanced morphometric techniques (36). However, the difference in the relationship between ADC and necrotic fraction between the two lines can, most likely, be explained by differences in tumor characteristics.

D-12 tumors developed a single region of massive necrosis with high ADC compared to the surrounding viable tissue. This ensured that an increasing fraction of water had high ADC with increasing necrotic fraction, leading to a high mean ADC of necrotic tumors. U-25 tumors, on the other hand, developed several small regions of necrosis distributed throughout the tissue. Consequently, although the necrotic fraction could be high, the area of the individual necrotic regions was generally small compared to the area of the necrotic region of D-12 tumors. This may have led to the lack of correlation between mean tumor ADC and necrotic fraction for several reasons. Firstly, the ADC of U-25 tumors may have been significantly influenced by partial volume effects, since the size of the necrotic regions often was comparable to or smaller than the voxel size of the MR images (Fig. 5d). Thus, viable tissue probably contributed to the ADC value of most pixels, even when located in regions that were identified as necrotic based on the histological sections, leading to de-

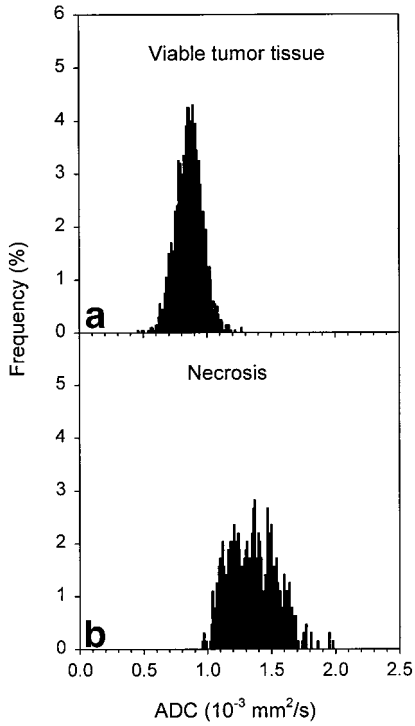

FIG. 7. ADC histograms of the viable (**a**) and necrotic (**b**) tissue of D-12 human melanoma xenograft tumors. The histograms are based on data of 8 tumors.

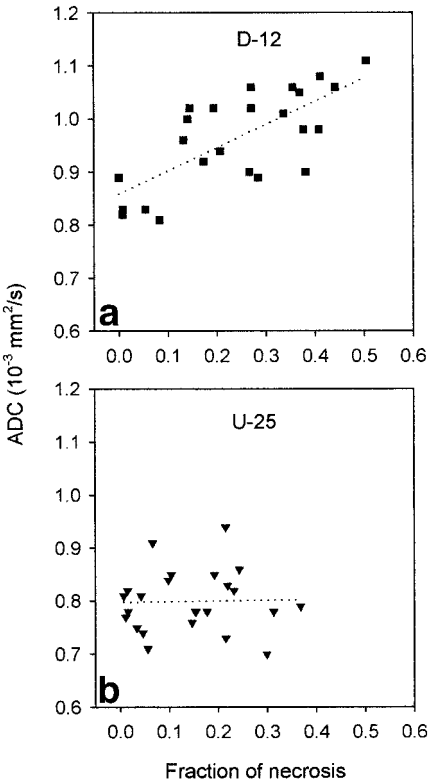

FIG. 8. Tumor ADC versus necrotic fraction of D-12 (**a**) and U-25 (**b**) human melanoma xenograft tumors. Each point represents the ADC of individual MR slices and the necrotic fraction of the corresponding histological section. The 3 central slices of 8 tumors, and hence 24 points, are presented for each line. ■, D-12 tumors; ▼, U-25 tumors. The stippled curves are fitted to the data by linear regression analysis.

creased difference in ADC between the necrotic and viable tissue. Secondly, small necrotic regions may have a large fraction of early stage necrosis compared to larger regions, since the distance to viable tumor tissue is smaller for these regions. The ADC of early stage necrosis is probably lower than that of massive necrosis, due to a larger content of cellular debris (23). This may also have led to a decreased difference in ADC between the necrotic and viable tissue, although for biological reasons not dependent on the spatial resolution. Consequently, a weaker and less detectable increase in ADC with increasing necrotic fraction may exist for the U-25 tumors than for the D-12 tumors.

Tumors may show large differences in cell density and necrotic fraction; parameters that may be indicative of tumor aggressiveness and response to therapy. Our work showed that such tumors may differ considerable with respect to ADCs, suggesting that DWI may be used clinically to assess the prognosis of cancer patients. Moreover, tumors develop both necrosis and reduced cell density of the viable tissue in response to many therapies. Thus, Braunschweiger et al. (35) noted a threefold decrease in the intracellular volume fraction of RIF-1 tumors and Steen et al. (37) found a sixfold decrease in the cell density of gliomas treated with chemotherapy. Differences in necrotic fraction and cell density during therapy may indicate different response. It is possible that DWI also can be useful in response evaluation (8–10). There may, however, occur changes in the extracellular matrix during treatment that influence the ADCs. Moreover, the structure and hence ADC of treatment induced necrosis may differ from that of natural occurring necrosis. ADC studies on tumors subjected to different therapies are therefore needed to verify the latter hypothesis.

In conclusion, the present results indicate that water ADCs can be used as measures of cell density and necrotic fraction of tumors developing no necrosis or a single region of massive necrosis. The viable tissue can easily be differentiated from necrosis in ADC maps of such tumors. On the other hand, the use of ADCs as measures of cell density and necrotic fraction of tumors developing several small necrotic regions is more problematic, since viable tissue and necrosis can be difficult to identify in ADC maps. To obtain information on cell density and necrosis of these tumors it is necessary that the spatial resolution of the ADC maps can be increased, e.g. by using thinner slices or a larger image matrix during DWI, without achieving a poor signal to noise ratio and, hence, unreliable pixel-by-pixel measurements of ADC.

ACKNOWLEDGMENTS

Financial support from The Norwegian Cancer Society is gratefully acknowledged.

REFERENCES

1. Tworek JA, Appelman HD, Singleton TP, Greenson JK. Stromal tumors of the jejunum and ileum. Mod Pathol 1997;10:200–209.
2. Rudolph P, Gloeckner K, Parwaresch R, Harms D, Schmidt D. Immunophenotype, proliferation, DNA ploidity, and biological behavior of gastrointestinal stromal tumors. a multivariate clinicopathologic study. Hum Pathol 1998;29:791–800.
3. Vallat-Decouvelaere AV, Dry SM, Fletcher CD. Atypical and malignant solitary fibrous tumors in extrathoracic locations: evidence of their comparability to intra-thoracic tumors. Am J Surg Pathol 1998;22: 1501–1511.
4. Majno G, Joris I. Apoptosis, oncosis, and necrosis. An overview of cell death. Am J Pathol 1995;146:3–15.
5. Field SB, Bleehen NM. Hyperthermia in the treatment of cancer. Cancer Treat Rev 1979;6:63–94.
6. Brown JM, Giaccia AJ. The unique physiology of solid tumors: opportunities (and problems) for cancer therapy. Cancer Res 1998;58:1408–1416.
7. Hendry JH, West CML. Apoptosis and mitotic cell death: their relative contributions to normal-tissue and tumour radiation response. Int J Radiat Biol 1997;71:709–719.
8. Zhao M, Pipe JG, Bonnett J, Evelhoch JL. Early detection of treatment response by diffusion-weighted ^{1}H-NMR spectroscopy in a murine tumour in vivo. Br J Cancer 1996;73:61–64.
9. Chenevert TL, McKeever PE, Ross BD. Monitoring early response of experimental brain tumors to therapy using diffusion magnetic resonance imaging. Clin Cancer Res 1997;3:1457–1466.
10. Poptani H, Puumalainen A-M, Gröhn OH, Loimas S, Kainulainen R, Ylä-Herttuala S, Kauppinen RA. Monitoring thymidine kinase and ganciclovir-induced changes in rat malignant glioma in vivo by nuclear magnetic resonance imaging. Cancer Gene Ther 1998;5:101–109.
11. Le Bihan D. Molecular diffusion, tissue microdynamics and microstructure. NMR Biomed 1995;8:375–386.
12. Szafer A, Zhong J, Gore JC. Theoretical model for water diffusion in tissues. Magn Reson Med 1995;33:697–712.

13. Mosely ME, Cohen Y, Mintorovitch J, Chileuitt L, Shimizu H, Kucharczyk J, Wendland MF, Weinstein PR. Early detection of regional cerebral ischemia in cats: comparison of diffusion- and T_2-weighted MRI and spectroscopy. Magn Reson Med 1990;14:330–346.
14. van Gelderen P, de Vleeschouwer MHM, DesPres D, Pekar J, van Zijl PCM, Moonen CTW. Water diffusion and acute stroke. Magn Reson Med 1994;31:154–163.
15. Duong TQ, Ackerman JJH, Ying HS, Neil JJ. Evaluation of extra- and intracellular apparent diffusion in normal and globally ischemic rat brain via ^{19}F NMR. Magn Reson Med 1998;40:1–13.
16. Kohno K, Hoehn-Berlage M, Mies G, Back T, Hossmann KA. Relationship between diffusion-weighted MR images, cerebral blood flow, and energy state in experimental brain infarction. Magn Reson Imaging 1995;13:73–80.
17. Mancuso A, Karibe H, Rooney WD, Zarow GJ, Graham SH, Weiner MW, Weinstein PR. Correlation of early reduction in the apparent diffusion coefficient of water with blood flow reduction during middle cerebral artery occlusion in rats. Magn Reson Med 1995;34:368–377.
18. Müller TB, Haraldseth O, Jones RA, Sebastiani G, Godtliebsen F, Lindboe CF, Unsgård G. Combined perfusion and diffusion weighted MR imaging in a rat model of reversible middle cerebral artery occlusion. Stroke 1995;26:451–457.
19. Tsuruda JS, Chew WM, Mosely ME, Norman D. Diffusion-weighted MR imaging of extraaxial tumors. Magn Reson Med 1991;19:316–320.
20. Maeda M, Kawamura Y, Tamagawa Y, Matsuda T, Itoh S, Kimura H, Iwasaki T, Hayashi N, Yamamoto K, Ishii Y. Intravoxel incoherent motion (IVIM) MRI of intracranial, extraaxial tumors and cysts. J Comput Assist Tomograph 1992;16:514–518.
21. Brunberg JA, Chenevert TL, McKeever PE, Ross DA, Junck LR, Muraszko KM, Dauser R, Pipe JG, Betley AT. In vivo MR determination of water diffusion coefficients and diffusion anisotropy. correlation with structural alteration in gliomas of the cerebral hemispheres. Am J Neuroradiol 1995;16:361–371.
22. Eis M, Els T, Hoehn-Berlage M. High resolution quantitative relaxation and diffusion MRI of three different experimental brain tumors in rat. Magn Reson Med 1995;34:835–844.
23. Maier CF, Paran Y, Bendel P, Rutt BK, Degani H. Quantitative diffusion imaging in implanted human breast tumors. Magn Reson Med 1997;37:576–581.
24. Sugahara T, Korogi Y, Kochi M, Ikushima I, Shigematu Y, Hirai T, Okuda T, Liang L, Ge Y, Komohara Y, Ushio Y, Takahashi M. Usefulness of diffusion-weighted MRI with echo-planar technique in the evaluation of cellularity in gliomas. J Magn Reson Imaging 1999;9:53–60.
25. Gupta RK, Sinha U, Cloughesy TF, Alger JR. Inverse correlation between choline magnetic resonance spectroscopy signal intensity and the apparent diffusion coefficient in human glioma. Magn Reson Med 1999;41:2–7.
26. Gupta RK, Cloughesy TG, Sinha U, Garakian J, Lazareff J, Rubino G, Becker DP, Vinters HV, Alger JR. Relationships between diffusion MRI, 1 H-MR spectroscopic imaging and quantitative histology in human glioma. In: Proceedings of the 7th Annual Meeting of the ISMRM, Philadelphia, 1999. p 429.
27. Rofstad EK. Orthotopic human melanoma xenograft model systems for studies of tumour angiogenesis, pathophysiology, treatment sensitivity, and metastatic pattern. Br J Cancer 1994;70:804–812.
28. Stilbs P, Mosely ME. Multicomponent self-diffusion measurement by the pulsed-gradient spin-echo method on standard Fourier transform NMR spectrometers. Chem Scripta 1980;15:176–179.
29. Brammer I, Jung H. Morphometry of irradiated tumors. In: Kallman RF, editor. Rodent tumor models in experimental cancer therapy. Elmsford, NY: Pergamon Press; 1987. p 97–100.
30. Cleveland GG, Chang DC, Hazlewood CF, Rorschach HE. Nuclear magnetic resonance measurement of skeletal muscle. Anisotropy of the diffusion coefficient of the intracellular water. Biophys J 1976;16:1043–1053.
31. Helmer KG, Dardzinski BJ, Sotak CH. The application of porous-media theory to the investigation of time-dependent diffusion in in vivo systems. NMR Biomed 1995;8:297–306.
32. Latour LL, Svoboda K, Mitra PP, Sotak CH. Time-dependent diffusion of water in a biological model system. Proc Natl Acad Sci USA 1994;91:1229–1233.
33. Helmer KG, Han S, Sotak CH. On the correlation between the water diffusion coefficient and oxygen tension in RIF-1 tumors. NMR Biomed 1998;11:120–130.
34. Bjørnæs I, Halsør EF, Skretting A, Rofstad EK. Measurement of the extracellular volume of human melanoma xenografts by contrast enhanced magnetic resonance imaging. Magn Reson Imaging 2000;18:41–48.
35. Braunschweiger PG, Schiffer L, Furmanski P. The measurement of extracellular water volumes in tissues by gadolinium modification of ^{1}H-NMR spin lattice (T_1) relaxation. Magn Reson Imaging 1986;4:285–291.
36. van der Sanden BPJ, Rijken PFJW, Heerschap A, Bernsen HJJA, van der Kogel AJ. In vivo ^{31}P magnetic resonance spectroscopy and morphometric analysis of the perfused vascular architecture of human xenografts in nude mice. Br J Cancer 1997;75:1432–1438.
37. Steen RG, Tamargo RJ, McGovern KA, Rajan SS, Brem H, Wehrle JP, Glickson JD. In vivo ^{31}P NMR spectroscopy of subcutaneous 9L gliosarcoma. effects of tumor growth and treatment with 1,3-Bis(2-chloroethyl)-1-nitrosourea on tumor bioenergetics and histology. Cancer Res 1998;48:676–681.